PHYSICAL REVIEW A **91**, 043821 (2015)

Accelerated rotation with orbital angular momentum modes

Christian Schulze,[1] Filippus S. Roux,[2] Angela Dudley,[2] Ronald Rop,[3] Michael Duparré,[1] and Andrew Forbes[2,4,*]
[1]*Institute of Applied Optics, Friedrich Schiller University, Fröbelstieg 1, 07743 Jena, Germany*
[2]*Council for Scientific and Industrial Research, P.O. Box 395, Pretoria 0001, South Africa*
[3]*Department of Physics, Egerton University, P.O. Box 536, Egerton 20115, Kenya*
[4]*School of Physics, University of the Witwatersrand, Johannesburg 2002, South Africa*

(Received 14 January 2015; published 13 April 2015)

We introduce a class of light field that angularly accelerates during propagation. We show that the acceleration (deceleration) may be controlled by adjustment of a single parameter, and tuned continuously, down to no acceleration at all. As the angular acceleration takes place in a bounded space, the azimuthal degree of freedom, such fields accelerate periodically as they propagate. Notably, the amount of angular acceleration is not limited by paraxial considerations, may be tailored for large accelerations over arbitrarily long distances, and can be engineered independently of the beam's spatial extent. We discuss how such angularly accelerating light fields can maintain the conservation of angular momentum through an energy exchange mechanism across the field.

DOI: 10.1103/PhysRevA.91.043821 PACS number(s): 42.25.Bs, 42.40.Jv, 42.60.Jf

I. INTRODUCTION

The concept of accelerating light at first appears incompatible with the fact that light travels at a constant speed and in a straight line. But it has been shown that if specific features of the fields are considered in isolation, then strange and counterintuitive propagation characteristics can be realized. Present examples all consider features of the field that appear to *transversely* accelerate as they propagate [1]. These include the now well-known Airy beams [2], whose intensity peak follows a parabolic path through space even if the centroid itself obeys rectilinear propagation. Such fields suffer from rapid deviation from the paraxial approximation due to the constantly changing propagation angle. Thus while they exhibit interesting transverse acceleration, which has seen them applied in a range of fields from particle manipulation [3], spatial-temporal beam control [4,5], and plasma control [6] to nonlinear optics [7–9], this deviation from the paraxial approximation is a limiting factor. More recently two-dimensional parabolic accelerating beams have been found to overcome some of these limitations, as well as nonparaxial transversely accelerating beams in the form of Weber beams [10,11], Mathieu beams [11], Bessel beams [12–14], vector beams [15–17], and beams with arbitrary transverse shapes [18]. Such beams have been demonstrated both with continuous waves and ultrashort pulses [19] and were shown to preserve their shape even in nonlinear media [20]. The accelerating properties are not limited to photons: some of the previously mentioned concepts have been implemented as nonoptical wave packets with electrons [21]. Nevertheless, by definition the transverse acceleration is always coupled to the lateral extent of the field: higher acceleration implies large propagation angles, and thus more of the transverse plane, which is an unbounded space, is used.

One way to overcome these limitations is to confine the motion to the azimuthal degree of freedom by creating rotating light fields. Since the azimuthal degree of freedom is bounded, the size of the field can be selected independent of the amount of rotation desired (one can spin about a circle indefinitely regardless of the circle radius). The theory for such rotating fields of constant angular velocity has been extensively developed [22] and generalized recently in the context of radial self-acceleration [23]. Such beams have been experimentally investigated in great detail [24–32]. The intensity maxima of these fields gyrate around the optical axis, forming a solenoidal shape, which has been used for the transport of trapped particles [33–35]. But since this motion is at a constant angular velocity, there is no angular acceleration.

Here we demonstrate controlled acceleration of a beam's rotation. Note that this type of acceleration is entirely different from the transverse acceleration discussed before. We tailor our "twisted light" (fields carrying orbital angular momentum) to have a nonlinear phase variation with azimuthal angle, which we show is the building block for *angular* accelerating light. The degree of nonlinearity determines the magnitude of the angular acceleration and deceleration, which may readily be tuned by adjusting a single parameter. This class of optical field has the advantages that the acceleration is not directly coupled to the size of the field and may be tuned to very high values, there is no limit on the amount of rotation that can be tolerated, and consequently the angular acceleration or deceleration may continue for arbitrarily long distances and used in applications where tight focusing is required, e.g., optical trapping and tweezing and optically driven flow for optofluidics.

II. THEORY

We recall that light fields with a phase factor of $\exp(i\ell\varphi)$, where φ is the azimuthal angle and ℓ the topological charge of the field, carry orbital angular momentum (OAM) of $\ell\hbar$ per photon [36]. Such fields are variously referred to as vortex or twisted light because of the helical phase fronts of helicity ℓ. Examples of such fields are found as the familiar Laguerre-Gaussian [37] and Bessel-Gaussian beams [38,39], and have been studied and applied in both the classical and quantum regimes. There is a phase singularity (and intensity null) at the center of the beam where a vortex of order ℓ is to be found. Figures 1(a)–1(c) show examples of such vortex phase profiles for $\ell = 1$, 2, and 3. These are isotropic vortex phase profiles,

---

[*] Corresponding author: aforbes1@csir.co.za

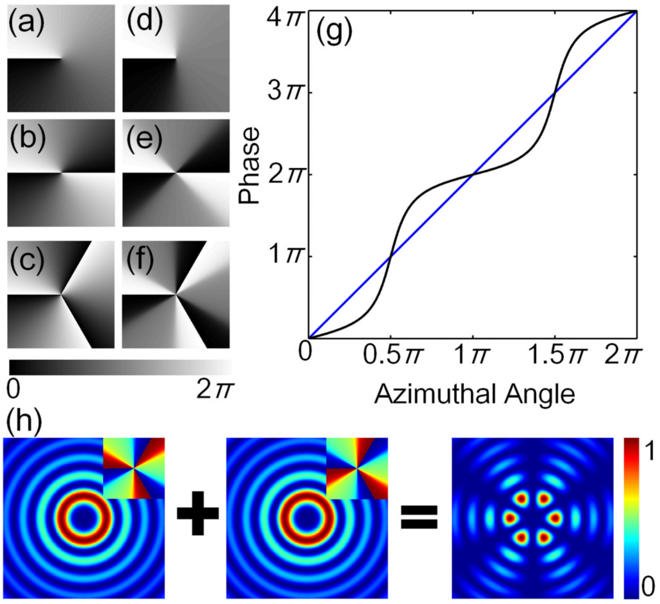

FIG. 1. (Color online) (a)–(c) Isotropic vortex phases for $\ell = 1, 2,$ and 3, respectively. (d)–(f) Anisotropic vortex phases for $\ell = 1, 2,$ and 3, respectively. (g) A plot of the phase as a function of azimuthal angle for an isotropic (blue) and an anisotropic (black) vortex of order $\ell = 2$. (h) Schematic showing the superposition of two Bessel beams as intensities (with anisotropic vortex phase as insets) and the resulting intensity petal structure, for $\ell = 3$.

and, pertinently, they vary linearly with the azimuthal angle, with slope ℓ, following $\psi(\varphi) = \ell\varphi$, where ψ is the phase.

A. Linear rotation

When superpositions of such isotropic vortex beams are created, they can be engineered [22,24–31] to produce nonrotationally symmetric intensity patterns that rotate at a constant angular velocity. This can, for instance, be done by adding two isotropic vortex beams with opposite azimuthal indices $\ell_1 = -\ell_2$ and slightly different propagation constants (slightly different values of k_z). Factoring out the parts that are different in the φ and z dependences of these two beams, we obtain

$$\begin{aligned} &\exp[i(\ell\varphi - z\Delta k_z)] + \exp[-i(\ell\varphi - z\Delta k_z)] \\ &\quad \propto \cos(\ell\varphi - z\Delta k_z), \end{aligned} \tag{1}$$

where $\Delta k_z = (k_{z1} - k_{z2})/2$. The orientation of the intensity profile of the superposition rotates as a function of propagation distance,

$$\phi(z) = \frac{z\Delta k_z}{\ell}, \tag{2}$$

where $\phi(z)$ represents the orientation of the intensity profile. This results in a constant angular velocity of

$$\frac{d\phi(z)}{dz} = \frac{\Delta k_z}{\ell}, \tag{3}$$

but no angular acceleration, since

$$\frac{d^2\phi(z)}{dz^2} = \ddot{\phi} = 0. \tag{4}$$

It is the linear azimuthal phase that restricts the motion to linear rotation. The linear rotation of the profile follows from that fact that the optical current (gradient of the phase profile times the intensity) [40], which governs the flow of the optical power, is constant as a function of the azimuthal angle for these isotropic phase profiles.

B. Nonlinear rotation

It thus follows that to obtain an angular acceleration of the beam profile one needs a nonlinear variation in the phase profile as a function of the azimuthal angle. This is visualized by the examples presented in Figs. 1(d)–1(f) for $\ell = 1, 2,$ and 3. To be a continuous function, the nonlinear phase profile must be a periodic function so that $\psi(0) = \psi(2\pi)$. As a result, the phase factor for a beam that would produce angular acceleration could, for example, have the form

$$\psi(\varphi) = \ell\varphi + \alpha\cos(\ell\varphi), \tag{5}$$

where α is an adjustable parameter that determines the magnitude of the acceleration. Note that the second derivative of $\psi(\varphi)$ in Eq. (5) is nonzero, which indicates angular (de)acceleration. For example, a superposition of the form

$$\begin{aligned} u &\propto \exp\{i[\psi(\varphi) + \Delta k_z z]\} + \exp\{-i[\psi(\varphi) + \Delta k_z z]\} \\ &= 2\cos[\psi(\varphi) + \Delta k_z z] \end{aligned} \tag{6}$$

will now have a stationary point in the field that varies nonlinearly with propagation distance: $\ell\phi(z) + \alpha\cos[\ell\phi(z)] = -\Delta k_z z$. This results in a nonconstant angular velocity of $\dot{\phi}(z) = -\Delta k_z/[\ell - \alpha\sin\ell\phi(z)]$, and also an angular acceleration since $\ddot{\phi} \neq 0$.

Plotting both the linear (isotropic) and nonlinear (anisotropic) phase variations together [Fig. 1(g)], we note that both are periodic about the azimuth.

C. Implementation

We create the desired anisotropic vortex fields [whose phase profiles are depicted in Figs. 1(d)–1(f)] by a superposition of two isotropic vortex beams with opposite helicities. Such a combination can be written in terms of nondiffracting fields as

$$\begin{aligned} u_{\mathrm{nl}}(r,\varphi,\theta) = A_\ell(r)[&\cos(\theta/2)\exp(i\ell\varphi) \\ &+ \sin(\theta/2)\exp(-i\ell\varphi)] \end{aligned} \tag{7}$$

at $z = 0$, where $A_\ell(r)$ is some radial (r) enveloping function and θ determines the morphology (anisotropy) of the optical vortex on the axis of the beam. The morphology parameter θ governs the relative weights of the two opposite topological charges. For $0 < \theta < \pi$ the overall topological charge is positive and for $\pi < \theta < 2\pi$ it is negative. By adding two such anisotropic nondiffracting vortex beams of differing phase velocities (k_z) and opposite morphology, the resulting field

$$\begin{aligned} u(r,\varphi,z) = {}& u_{\mathrm{nl}}(r,\varphi,\theta)\exp(ik_{z1}z) \\ &+ u_{\mathrm{nl}}(r,\varphi,\pi - \theta)\exp(ik_{z2}z) \end{aligned} \tag{8}$$

will have a structured pattern (petals) in the azimuth (φ) that rotates during propagation, with an angular velocity that depends on z. This is shown schematically in Fig. 1(h) where the two anisotropic fields result in a petal-like structure about the azimuth.

For convenience, and without any loss of generality, we will discuss the implementation in the context of Bessel beams so that $A_\ell(r) = \mathrm{J}_\ell(rk_r)$. Such fields are convenient as their radial wave vector (k_r), and consequently k_z, are easily controlled with digital holograms, and are related by

$$k_z = \sqrt{k^2 - k_r^2}, \tag{9}$$

where $k = 2\pi/\lambda$ is the wave number and λ is the wavelength of the light. The superposition field Eq. (7) then becomes

$$\begin{aligned} u(r,\varphi,z) = {} & \mathrm{J}_\ell(rk_{r1})[\cos(\theta/2)\exp(i\ell\varphi) \\ & + \sin(\theta/2)\exp(-i\ell\varphi)]\exp(ik_{z1}z) \\ & + \mathrm{J}_\ell(rk_{r2})[\sin(\theta/2)\exp(i\ell\varphi) \\ & + \cos(\theta/2)\exp(-i\ell\varphi)]\exp(ik_{z2}z). \end{aligned} \tag{10}$$

The optical field in Eq. (10) consists of the superposition of four Bessel beams—two pairs with slightly different values of k_r (and therefore slightly different values of k_z). Each pair is a superposition of two Bessel beams with opposite azimuthal indices that produces an anisotropic optical vortex in the center of the beam. This ensures both requirements: nonlinear but periodic phase variation about the azimuth, as shown in Fig. 1(g). It is easy to show that the angular position of each petal rotates during propagation, following

$$\phi(z) = \frac{1}{2|\ell|}\arctan\left[\frac{\cos(\theta)\sin(z\Delta)}{\sin(\theta)+\cos(z\Delta)}\right], \tag{11}$$

where $\Delta = k_{z2} - k_{z1}$. We note that the morphology parameter θ acts as a tuning parameter that determines the degree of nonlinearity, and therefore also the angular velocity of the rotation. The latter can be shown to be

$$\dot{\phi} = \frac{\Delta}{2|\ell|}\frac{\cos(2\theta)}{1+\sin(2\theta)\cos(z\Delta)}, \tag{12}$$

from which we may immediately find the angular acceleration:

$$\ddot{\phi} = \frac{\Delta^2}{4|\ell|}\frac{\sin(2\theta)\sin(z\Delta)}{[1+\sin(\theta)\cos(z\Delta)]^2}. \tag{13}$$

III. EXPERIMENT

In our experiment a linearly polarized, single wavelength ($\lambda = 632.8$ nm) helium-neon laser (Melles Griot) with a power of 10 mW was expanded and collimated by a telescope ($f_{\mathrm{L1}} = 15$ mm and $f_{\mathrm{L2}} = 125$ mm) to approximate a plane wave. The plane wave illuminated a HoloEye Pluto spatial light modulator (SLM) (1080×1920 pixels), with a pixel size of 8 μm and which was calibrated for a wavelength of 633 nm. The SLM was addressed with holograms of a ring-slit aperture [41,42], encoded via complex amplitude modulation [43]. Two ring-slit apertures were used, each encoded with an anisotropic azimuthal phase variation of opposite topological charge, respectively, with radii $R_1 = 179$ pixels (1432 μm) and $R_2 = 195$ pixels (1560 μm) and $d = 11$ pixels (88 μm) in width.

The Fourier transform of the field at the plane of the SLM was obtained with the use of a lens: $f_{\mathrm{L3}} = 200$ mm. In this way we obtained the superposition of two Bessel beams with opposite topological charges and with $k_{r1} = 28428.1\ \mathrm{m}^{-1}$ and $k_{r2} = 30\,969.2\ \mathrm{m}^{-1}$. A Bessel beam thus created is valid over a finite propagation distance $z_{\max} = 2\pi\omega_0/\lambda k_r$, shown as the shaded red region in Fig. 2(a). The resulting beam profile was magnified with a 10× objective, which also acted as an aperture to select only the first diffraction order which was captured on a CCD camera (Point Grey fire-wire CCD). To extract the petal position from the captured camera images, the measured Bessel beams were compared to simulated beams with the same number of petals, which were adapted in spatial scale. The comparison was achieved in a quantitative manner by evaluating a two-dimensional cross-correlation coefficient when rotating the simulated patterns with respect to the measured beam. The correct rotation angle of the measured beam was found from a maximum of the correlation function. To avoid ambiguities in the form of a multiple number of correlation maxima, the simulated pattern was rotated within the interval of 0° to $180^\circ/\ell$. The fidelity of the process was improved by iteratively refining the interval limits until a chosen accuracy was achieved, which was 0.1° in the experiments.

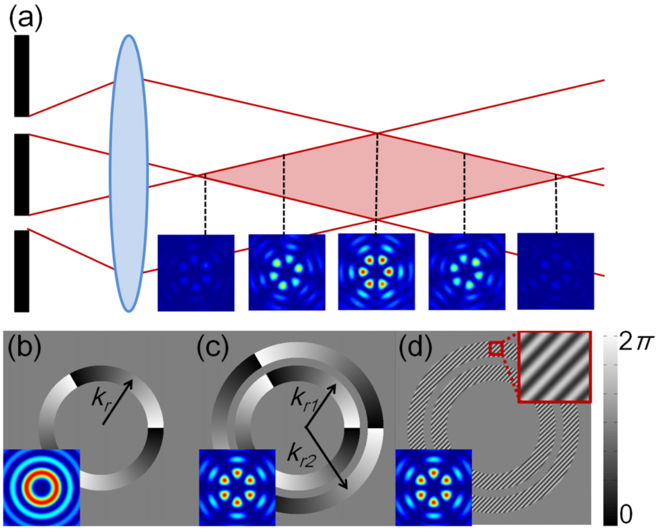

FIG. 2. (Color online) (a) A Bessel beam can be formed by illuminating a ring slit placed in the Fourier plane of a lens. (b) To create a field comprising a single radial wave vector k_r, a single ring slit is illuminated. Superpositions of isotropic Bessel beams with differing radial wave vectors simply require multiple ring slits as shown in (c), while anisotropic superpositions require amplitude modulation inside each of these ring slits, as shown in (d). The corresponding intensities produced for each case are shown in the insets.

IV. RESULTS

A. Angular velocity and acceleration

The intensity patterns were recorded during propagation and are shown for the linear and nonlinear cases in Figs. 3(a) and 3(b) for superpositions of $\ell = 1$ and $\ell = 3$, respectively (see the movies in the Supplemental Material [44]). The predicted and measured angular position during propagation for selected values of the morphology parameter θ are shown

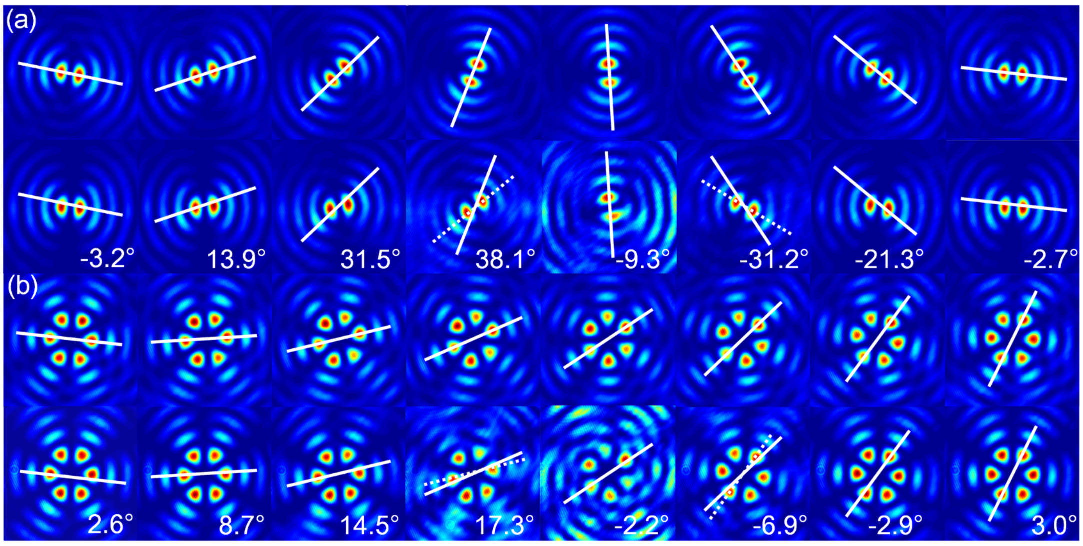

FIG. 3. (Color online) The intensity images in the top rows of (a) and (b) show the petal rotation at a fixed rate $\theta = 0$, while the bottom rows show the nonlinear rotation $\theta = \pi/3$, for (a) $\ell = 1$ and (b) $\ell = 3$. The solid white lines indicate the movement of the petals in the linear case and are overlaid on the nonlinear images for reference. The angular difference between the two cases (linear and nonlinear) is given as text in each frame. The columns represent increasing propagation distances sampled from the zoomed-in data set of Fig. 4. The maximum beam intensities in each frame were normalized to unity to aid comparison.

in Figs. 4(a) and 4(b), for $\ell = 1$ and $\ell = 3$, respectively, where the theoretical predictions are validated by the experimental results.

More importantly, the angular velocity and acceleration of these fields have been confirmed experimentally, with results shown in Fig. 5 for $\ell = 1$ and $\ell = 3$. As the field propagates in the positive z direction, so the petal pattern rotates. The angular velocity of this rotation changes during propagation according to Eq. (12), following an oscillatory evolution. This is evident in Figs. 5(a) and 5(b). The fact that the angular velocity is oscillatory implies that the beam experiences both acceleration and deceleration during propagation, which is verified experimentally in Figs. 5(c) and 5(d).

B. Conservation of angular momentum

One may rightfully ask: How does an optical field that undergoes angular accceleration maintain the conservation of angular momentum? The answer to this question reveals an interesting feature of such an optical field. It turns out that the total optical field may be viewed as two separate structures that perform independent rigid rotations. The dominant structure with the petal pattern is located in the central region of the beam. The other structure, which has rings, has a lower average intensity and is spread over a larger area. Power is periodically exchanged between the two structures. Each of these structures gains and loses power in a manner that is directly coupled to their angular acceleration. When one accelerates, the other one decelerates and power is transferred from the accelerating one to the decelerating one. In other words, a fast-rotating field appears dim, while a slow-rotating field appears bright. This exchange is measured and plotted in Figs. 6(a) and 6(b). Due to this exchange of power and the fact that the two structures take turns to accelerate or decelerate, the angular momentum of the entire optical field can remain constant.

We now provide a more careful analysis of this behavior. The intensity of the field in Eq. (10) can be expressed in terms of the sum and difference of the two terms,

$$\begin{aligned}\mathcal{I}(r,\varphi,z) &= u(r,\varphi,z)u^*(r,\varphi,z)\\ &= \mathcal{I}_\Sigma(r,\varphi,z) + \mathcal{I}_\Delta(r,\varphi,z)\\ &= \tfrac{1}{2}R_{\mathrm{s}}^2(r)[1+\cos(2\ell\varphi - 2\ell\Theta_{\mathrm{s}})]\\ &\quad \times [1+\sin(\theta)\cos(z\Delta)]\\ &\quad + \tfrac{1}{2}R_{\mathrm{d}}^2(r)[1+\cos(2\ell\varphi - 2\ell\Theta_{\mathrm{d}})]\\ &\quad \times [1-\sin(\theta)\cos(z\Delta)],\end{aligned} \tag{14}$$

where

$$R_{\mathrm{s}}(r) = \mathrm{J}_\ell(rk_{r1}) + \mathrm{J}_\ell(rk_{r2}), \tag{15}$$

$$R_{\mathrm{d}}(r) = \mathrm{J}_\ell(rk_{r1}) - \mathrm{J}_\ell(rk_{r2}), \tag{16}$$

$$\Theta_{\mathrm{s}} = -\frac{1}{2\ell}\arctan\left[\frac{\cos(\theta)\sin(z\Delta)}{\sin(\theta)+\cos(z\Delta)}\right], \tag{17}$$

$$\Theta_{\mathrm{d}} = \frac{1}{2\ell}\arctan\left[\frac{\cos(\theta)\sin(z\Delta)}{\sin(\theta)-\cos(z\Delta)}\right], \tag{18}$$

$$\Delta = k_{z2} - k_{z1}. \tag{19}$$

The sum term [first term in Eq. (14)] represents the part that dominates in the central part of the beam (the inner region, or petals), while the difference term [second term in Eq. (14)] covers a larger area of the beam (the outer region, or rings). From Eq. (14) we see that the sum and difference terms are each modulated by a φ-dependent factor and a z-dependent factor. The z-dependent factors of the two terms are out of phase so that the sum and the difference terms alternate in brightness. The φ-dependent factors represent a z-dependent orientation, given by Eqs. (17) and (18) for the sum and difference terms,

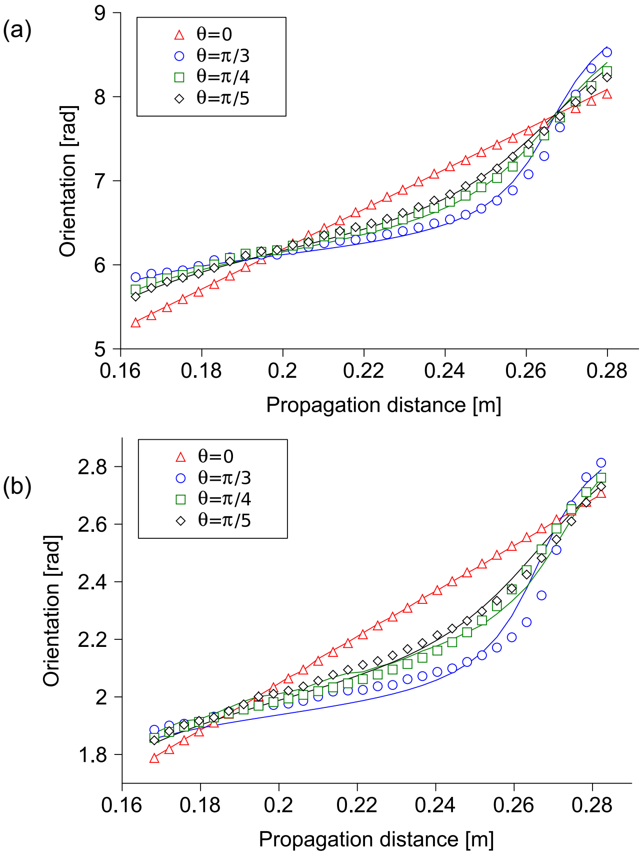

FIG. 4. (Color online) The rotation angle (ϕ) of the petal structure as the field propagated. The measured data (symbols) are shown together with the theoretical predictions (lines) for various values of the control parameter θ, from 0 (red), $\pi/5$ (black), $\pi/4$ (green), to $\pi/3$ (blue). The rotation rate was observed to transition from constant ($\theta = 0$) to highly nonlinear ($\theta = \pi/3$). Results are shown for two different topological charge values of (a) $\ell = 1$ and (b) $\ell = 3$.

respectively. The rates at which these orientations change (angular velocity) are given by

$$\partial_z \Theta_s = -\left(\frac{\Delta}{2\ell}\right) \frac{\cos(\theta)}{1 + \sin(\theta)\cos(z\Delta)}, \tag{20}$$

$$\partial_z \Theta_d = -\left(\frac{\Delta}{2\ell}\right) \frac{\cos(\theta)}{1 - \sin(\theta)\cos(z\Delta)}, \tag{21}$$

and the angular accelerations are found to be

$$\partial_z^2 \Theta_s = -\left(\frac{\Delta^2}{4\ell}\right) \frac{\sin(2\theta)\sin(z\Delta)}{[1 + \sin(\theta)\cos(z\Delta)]^2}, \tag{22}$$

$$\partial_z^2 \Theta_d = \left(\frac{\Delta^2}{4\ell}\right) \frac{\sin(2\theta)\sin(z\Delta)}{[1 - \sin(\theta)\cos(z\Delta)]^2}. \tag{23}$$

Comparing Eqs. (22) and (23) with the two terms in Eq. (14), we see that the angular accelerations of the two parts are inversely proportional to the squares of their z-dependent intensity modulations. Therefore, the one that rotates slowly is always brighter than the other one, which rotates fast.

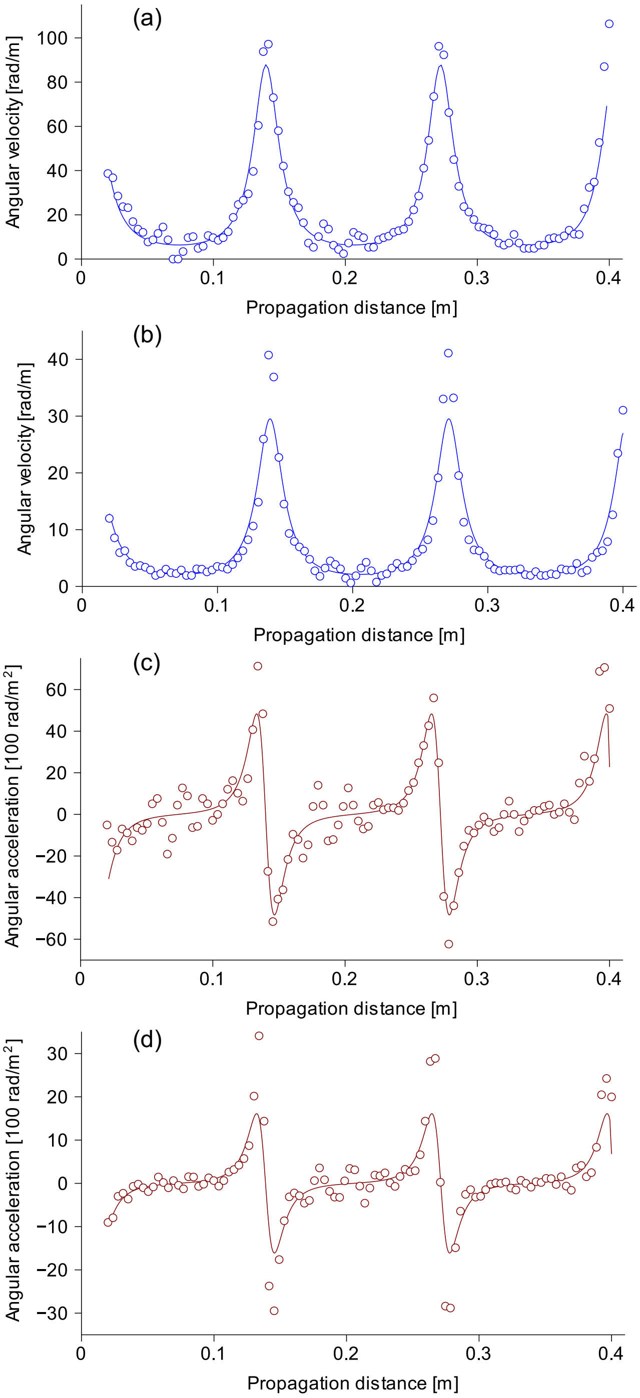

FIG. 5. (Color online) The nonlinear azimuthal phase of the anisotropic beam results in a rotation angle that varies nonlinearly with propagation distance. This varying angular velocity imparts angular acceleration to the field. The nonconstant angular velocity is shown in (a) and (b) for $\ell = 1$ and $\ell = 3$, respectively, while the resultant angular acceleration for these examples is shown in (c) and (d). The measured data (circles) are in good agreement with the theoretical predictions (solid curve).

C. Power exchange

The fact that the optical power in the two terms in Eq. (14) varies as a function of propagation distance implies that they exchange power during propagation. To understand this

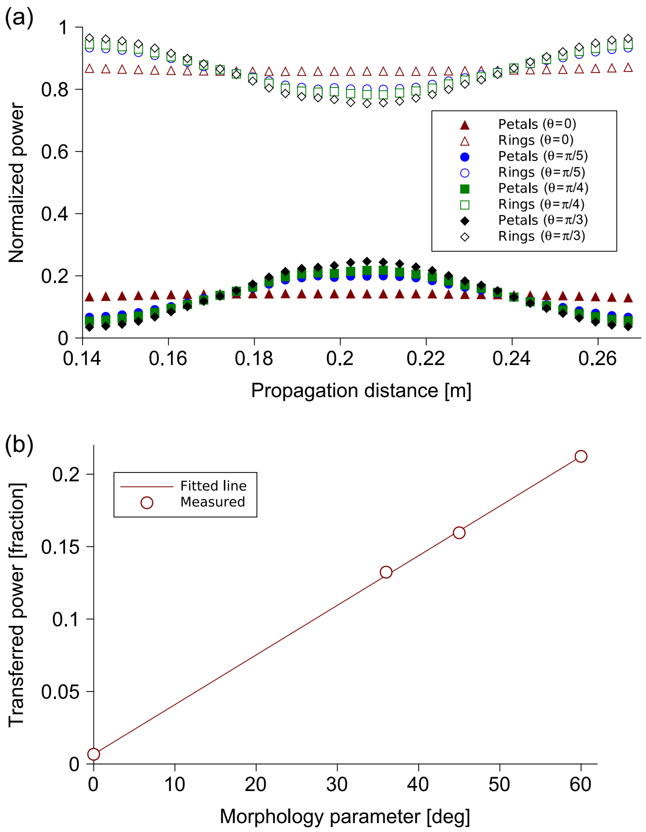

FIG. 6. (Color online) As the beam accelerates the energy in the inner region (petals) is transported to the outer region (rings). This process is reversed during deceleration. Because the field oscillates between the two cases during propagation, there is a continuous flow of energy in and out of the central petal structure of the field. (a) The normalized energy in the two regions (petals and rings) of the field during propagation for $\theta = 0$ (red), $\theta = \pi/5$ (black), $\theta = \pi/4$ (green), and $\theta = \pi/3$ (blue). (b) The measured maximum fractional energy exchange as a function of θ. All data are for the $\ell = 3$ case.

exchange we use the intensity transport equation [45]

$$\partial_z \mathcal{I} = \frac{1}{k}\nabla \cdot \mathbf{J}, \tag{24}$$

where

$$\mathbf{J} = \mathcal{I}\,\nabla\psi, \tag{25}$$

is the optical current [40], with ψ being the phase of the optical field. The optical current is proportional to the Poynting vector in the paraxial limit. The intensity transport equation is a statement of energy (power) conservation: the change in the local intensity is balanced by the divergence of the optical current. If there were no exchange of optical power between the sum and difference terms, each would have obeyed the intensity transport equation separately. Instead what we find is the following:

$$\partial_z \mathcal{I} = \partial_z \mathcal{I}_\Sigma + \partial_z \mathcal{I}_\Delta = \frac{1}{k}\nabla \cdot \mathbf{J}_\Sigma + \frac{1}{k}\nabla \cdot \mathbf{J}_\Delta + \mathcal{V}, \tag{26}$$

where $\mathcal{I}_\Sigma$ and $\mathcal{I}_\Delta$ are the intensities of the sum and difference, as defined in Eq. (14), $\mathbf{J}_\Sigma$ and $\mathbf{J}_\Delta$ are the optical currents associated with the sum and difference, given by

$$\begin{aligned} \mathbf{J}_\Sigma &= -\mathcal{I}_\Sigma\, \beta_0\, \hat{z} \\ \mathbf{J}_\Delta &= -\mathcal{I}_\Delta\, \beta_0\, \hat{z}, \end{aligned} \tag{27}$$

with $\beta_0 = (k_{z1} + k_{z2})/2$, and $\mathcal{V}$ is a coupling term given by

$$\begin{aligned} \mathcal{V} = &-\frac{1}{2k}\left[R_\mathrm{d}\partial_r^2 R_\mathrm{s} - R_\mathrm{s}\partial_r^2 R_\mathrm{d}\right] \\ &\times[1 + \sin(\theta)\cos(2\ell\varphi)]\sin(z\Delta + \Theta_c) \end{aligned} \tag{28}$$

with

$$\Theta_c = \arctan\left[\frac{\cos(\theta)\sin(2\ell\varphi)}{\sin(\theta) + \cos(2\ell\varphi)}\right]. \tag{29}$$

Since the coupling term contains both R_s and R_d in each term, it is responsible for the exchange of power between the sum and difference terms during propagation.

V. DISCUSSION

The experimentally recorded spatial profiles in the bottom rows of Figs. 3(a) and 3(b) demonstrate nonlinear rotation when compared with the case where the same fields rotate at a constant rate. This is observed by noting that the solid white lines that intersect two geometrically opposite intensity peaks in the top rows of Figs. 3(a) and 3(b) no longer intersect these intensity peaks in the bottom rows. Instead, there is an angular deviation with respects to the solid white line, illustrating that these fields have rotated either faster or more slowly than those presented in the top rows. Similarly, this transition from an already studied, constant, linear rotation to a new, accelerating, nonlinear rotation is depicted graphically in Fig. 4. Here, it is evident that the rotation of these fields can be tuned from being linear (constant) to being highly nonlinear (accelerating), by increasing the morphology parameter θ, defined in Eq. (7).

The angular velocity of these experimentally generated fields changes rapidly as they propagate, speeding up and slowing down, reaching very high angular velocities. This changing angular velocity [depicted in Figs. 5(a) and 5(b)] implies an angular acceleration [Figs. 5(c) and 5(d)], the origin of which resides in the phase structure of the superposition field. Since the angular velocity is oscillatory, the beam experiences both acceleration and deceleration during propagation. The magnitude of the angular velocity [Eq. (12)] and angular acceleration [Eq. (13)] is affected by both the topological charge (ℓ) of the beams in the superposition, as well as the difference in their phase velocities. The tuning (morphology) parameter θ determines whether the field will accelerate at all, and to what extent.

Previously studied rotating fields are recovered by setting $\theta = 0$ or $\theta = \pi$, since Eq. (7) then reduces to either one of the two OAM fields having linear azimuthal phase variation. In both cases, the petals rotate at a constant angular velocity, given by $\dot{\phi} = \Delta/2\ell$. Such fields, having no acceleration, have been studied in detail previously [24–32] and represent only a special case of the more general angularly accelerating light, described here.

The class of field reported here has some attractive properties. First, we point out that the azimuthal degree of freedom (where the accelerating motion takes place) is bounded and periodic. This means that the beam may continue to spin and angularly accelerate without changing size. This is in sharp contrast to transversely accelerating light where the transverse plane is unbounded: more acceleration means a larger portion of the plane, and consequently ever larger beam sizes. This is a fundamental property of transversely accelerating light since the peak intensity follows a parabolic caustic (away from the centroid) while the centroid itself remains rectilinear in propagation. Second, as a consequence of the above, very large acceleration values may be realized with angularly accelerating light, even when the field is tightly focused, or the field size is small. Such fields will have obvious applications in the optical control of microparticles [46–48] and may even be extended to the nonoptical domain [49] and nonlinear propagation [50,51] to explore additional physical processes.

VI. CONCLUSION

A concept for the angular acceleration of light is outlined and experimentally demonstrated. Our approach makes use of superpositions of OAM fields created with digital holograms. We show that the magnitude of the angular acceleration of these fields can be tuned continuously with the aid of a single morphology parameter. These fields have advantageous features that overcome previous disadvantages of transversely accelerating light: their feature sizes are not dictated by the degree of acceleration, the angular extent of the acceleration does not influence the paraxial nature of the field (the entire azimuthal degree of freedom can be used), and they can be engineered to extend over arbitrarily long distances. Given the interest and applications of transversely accelerating light, one can envisage many uses for this class of angular accelerating light, for example, in studies of the driving flow of optofluidic systems and accelerating matter waves.

[1] M. A. Bandres, I. Kaminer, M. Mills, B. Rodríguez-Lara, E. Greenfield, M. Segev, and D. N. Christodoulides, Accelerating optical beams, Opt. Photon. News **24**, 30 (2013).

[2] G. A. Siviloglou, J. Broky, A. Dogariu, and D. N. Christodoulides, Observation of accelerating airy beams, Phys. Rev. Lett. **99**, 213901 (2007).

[3] J. Baumgartl, M. Mazilu, and K. Dholakia, Optically mediated particle clearing using airy wavepackets, Nat. Photonics **2**, 675 (2008).

[4] A. Chong, W. H. Renninger, D. N. Christodoulides, and F. W. Wise, Airy-Bessel wave packets as versatile linear light bullets, Nat. Photonics **4**, 103 (2010).

[5] H. Valtna-Lukner, P. Bowlan, M. Lõhmus, P. Piksarv, R. Trebino, and P. Saari, Direct spatiotemporal measurements of accelerating ultrashort Bessel-type light bullets, Opt. Express **17**, 14948 (2009).

[6] P. Polynkin, M. Kolesik, J. V. Moloney, G. A. Siviloglou, and D. N. Christodoulides, Curved plasma channel generation using ultraintense airy beams, Science **324**, 229 (2009).

[7] I. Dolev, I. Kaminer, A. Shapira, M. Segev, and A. Arie, Experimental observation of self-accelerating beams in quadratic nonlinear media, Phys. Rev. Lett. **108**, 113903 (2012).

[8] I. Kaminer, M. Segev, and D. N. Christodoulides, Self-accelerating self-trapped optical beams, Phys. Rev. Lett. **106**, 213903 (2011).

[9] A. Lotti, D. Faccio, A. Couairon, D. G. Papazoglou, P. Panagiotopoulos, D. Abdollahpour, and S. Tzortzakis, Stationary nonlinear airy beams, Phys. Rev. A **84**, 021807 (2011).

[10] M. A. Bandres and B. Rodríguez-Lara, Nondiffracting accelerating waves: Weber waves and parabolic momentum, New J. Phys. **15**, 013054 (2013).

[11] P. Zhang, Y. Hu, T. Li, D. Cannan, X. Yin, R. Morandotti, Z. Chen, and X. Zhang, Nonparaxial Mathieu and Weber accelerating beams, Phys. Rev. Lett. **109**, 193901 (2012).

[12] I. D. Chremmos and N. K. Efremidis, Nonparaxial accelerating Bessel-like beams, Phys. Rev. A **88**, 063816 (2013).

[13] J. Zhao, P. Zhang, D. Deng, J. Liu, Y. Gao, I. D. Chremmos, N. K. Efremidis, D. N. Christodoulides, and Z. Chen, Observation of self-accelerating Bessel-like optical beams along arbitrary trajectories, Opt. Lett. **38**, 498 (2013).

[14] I. D. Chremmos, Z. Chen, D. N. Christodoulides, and N. K. Efremidis, Bessel-like optical beams with arbitrary trajectories, Opt. Lett. **37**, 5003 (2012).

[15] I. Kaminer, R. Bekenstein, J. Nemirovsky, and M. Segev, Nondiffracting accelerating wave packets of Maxwell's equations, Phys. Rev. Lett. **108**, 163901 (2012).

[16] M. A. Bandres, M. A. Alonso, I. Kaminer, and M. Segev, Three-dimensional accelerating electromagnetic waves, Opt. Express **21**, 13917 (2013).

[17] P. Aleahmad, M.-A. Miri, M. S. Mills, I. Kaminer, M. Segev, and D. N. Christodoulides, Fully vectorial accelerating diffraction-free Helmholtz beams, Phys. Rev. Lett. **109**, 203902 (2012).

[18] A. Ruelas, J. A. Davis, I. Moreno, D. M. Cottrell, and M. A. Bandres, Accelerating light beams with arbitrarily transverse shapes, Opt. Express **22**, 3490 (2014).

[19] F. Courvoisier, A. Mathis, L. Froehly, R. Giust, L. Furfaro, P. A. Lacourt, M. Jacquot, and J. M. Dudley, Sending femtosecond pulses in circles: highly nonparaxial accelerating beams, Opt. Lett. **37**, 1736 (2012).

[20] P. Zhang, Y. Hu, D. Cannan, A. Salandrino, T. Li, R. Morandotti, X. Zhang, and Z. Chen, Generation of linear and nonlinear nonparaxial accelerating beams, Opt. Lett. **37**, 2820 (2012).

[21] N. Voloch-Bloch, Y. Lereah, Y. Lilach, A. Gover, and A. Arie, Generation of electron Airy beams, Nature (London) **494**, 331 (2013).

[22] J. Tervo and J. P. Turunen, Rotating scale-invariant electromagnetic fields, Opt. Express **9**, 9 (2001).

[23] C. Vetter, T. Eichelkraut, M. Ornigotti, and A. Szameit, Generalized radially self-accelerating helicon beams, Phys. Rev. Lett. **113**, 183901 (2014).

[24] V. V. Kotlyar, S. N. Khonina, R. V. Skidanov, and V. A. Soifer, Rotation of laser beams with zero of the orbital angular momentum, Opt. Commun. **274**, 8 (2007).

[25] S. Chávez-Cerda, G. S. McDonald, and G. H. C. New, Nondiffracting beams: Traveling, standing, rotating and spiral waves, Opt. Commun. **123**, 225 (1996).

[26] E. Abramochkin, N. Losevsky, and V. Volostnikov, Generation of spiral-type laser beams, Opt. Commun. **141**, 59 (1997).

[27] P. Pääkkönen, J. Lautanen, M. Honkanen, M. Kuittinen, J. Turunen, S. N. Khonina, V. V. Kotlyar, V. A. Soifer, and

A. T. Friberg, Rotating optical fields: Experimental demonstration with diffractive optics, J. Mod. Opt. **45**, 2355 (1998).

[28] Y. Y. Schechner, R. Piestun, and J. Shamir, Wave propagation with rotating intensity distributions, Phys. Rev. E **54**, R50 (1996).

[29] V. R. Daria, D. Z. Palima, and J. Glückstad, Optical twists in phase and amplitude, Opt. Express **19**, 476 (2011).

[30] S. Franke-Arnold, J. Leach, M. J. Padgett, V. E. Lembessis, D. Ellinas, A. J. Wright, J. M. Girkin, P. Ohberg, and A. S. Arnold, Optical ferris wheel for ultracold atoms, Opt. Express **15**, 8619 (2007).

[31] R. Rop, A. Dudley, C. López-Mariscal, and A. Forbes, Measuring the rotation rates of superpositions of higher-order Bessel beams, J. Mod. Opt. **59**, 259 (2012).

[32] R. Rop, I. A. Litvin, and A. Forbes, Generation and propagation dynamics of obstructed and unobstructed rotating orbital angular momentum-carrying helicon beams, J. Opt. **14**, 035702 (2012).

[33] S.-H. Lee, Y. Roichman, and D. G. Grier, Optical solenoid beams, Opt. Express **18**, 6988 (2010).

[34] E. R. Shanblatt and D. G. Grier, Extended and knotted optical traps in three dimensions, Opt. Express **19**, 5833 (2011).

[35] J. E. Curtis and D. G. Grier, Modulated optical vortices, Opt. Lett. **28**, 872 (2003).

[36] L. Allen, M. J. Padgett, and M. Babiker, The orbital angular momentum of light, Prog. Opt. **39**, 291 (1999).

[37] A. M. Yao and M. J. Padgett, Orbital angular momentum: Origins, behavior and applications, Adv. Opt. Photon. **3**, 161 (2011).

[38] D. McGloin and K. Dholakia, Bessel beams: Diffraction in a new light, Contemp. Phys. **46**, 15 (2005).

[39] M. Mazilu, D. J. Stevenson, F. Gunn-Moore, and K. Dholakia, Light beats the spread: Non-diffracting beams, Laser Photon. Rev. **4**, 529 (2010).

[40] M. V. Berry, Optical currents, J. Opt. A: Pure Appl. Opt. **11**, 094001 (2009).

[41] J. Turunen, A. Vasara, and A. T. Friberg, Holographic generation of diffraction-free beams, Appl. Opt. **27**, 3959 (1988).

[42] R. Vasilyeu, A. Dudley, N. Khilo, and A. Forbes, Generating superpositions of higher–order Bessel beams, Opt. Express **17**, 23389 (2009).

[43] V. Arrizón, U. Ruiz, R. Carrada, and L. A. González, Pixelated phase computer holograms for the accurate encoding of scalar complex fields, J. Opt. Soc. Am. A **24**, 3500 (2007).

[44] See Supplemental Material at http://link.aps.org/supplemental/10.1103/PhysRevA.91.043821 for videos.

[45] M. R. Teague, Irradiance moments: their propagation and use for unique retrieval of phase, J. Opt. Soc. Am. **72**, 1199 (1982); Deterministic phase retrieval: A Green's function solution, **73**, 1434 (1983); Image formation in terms of the transport equation, **2**, 2019 (1985).

[46] D. Palima and J. Glückstad, Gearing up for optical microrobotics: Micromanipulation and actuation of synthetic microstructures by optical forces, Laser Photon. Rev. **7**, 478 (2013).

[47] K. Dholakia and T. Čižmár, Shaping the future of manipulation, Nat. Photonics **5**, 335 (2011).

[48] M. Padgett and R. Bowman, Tweezers with a twist, Nat. Photonics **5**, 343 (2011).

[49] V. Grillo, E. Karimi, G. C. Gazzadi, S. Frabboni, M. R. Dennis, and R. W. Boyd, Generation of nondiffracting electron Bessel beams, Phys. Rev. X **4**, 011013 (2014).

[50] A. S. Desyatnikov, A. A. Sukhorukov, and Y. S. Kivshar, Azimuthons: Spatially modulated vortex solitons, Phys. Rev. Lett. **95**, 203904 (2005).

[51] A. Bekshaev and M. Soskin, Rotational transformations and transverse energy flow in paraxial light beams: Linear azimuthons, Opt. Lett. **31**, 2199 (2006).